2014

Full of Hot Air: Heat Flow at the Medicine Lake Volcano Hot Spot, Modoc County, California

Katrina D. Gelwick
Oberlin College

Repository Citation

Gelwick, Katrina D., "Full of Hot Air: Heat Flow at the Medicine Lake Volcano Hot Spot, Modoc County, California" (2014). *Honors Papers*. 288.
https://digitalcommons.oberlin.edu/honors/288

FULL OF HOT AIR:
HEAT FLOW AT THE MEDICINE LAKE VOLCANO HOT SPOT, MODOC COUNTY, CALIFORNIA

Katrina D. Gelwick
Honors Thesis
April 2014

Advisors:

F. Zeb Page
Department of Geology, Oberlin College, Oberlin, OH

Steven E. Ingebritsen
U.S. Geological Survey, Menlo Park, CA

Submitted in partial fulfillment of the requirements for a Bachelor of Arts degree with Honors in Geology from Oberlin College, Oberlin, Ohio

Abstract

Changes in volcanic hydrothermal systems can shed light on the physical processes associated with volcanic unrest such as changes in an underlying magma body. The U.S. Geological Survey recently implemented an experimental hydrothermal monitoring network throughout the Cascade volcanic arc. Despite being ranked as the 12th highest threat among all Cascade volcanoes, Medicine Lake Volcano in northeastern California is considered under-monitored. The primary hydrothermal-monitoring site at Medicine Lake Volcano is a weak fumarole contained within a small area of heated ground, called the Hot Spot, located near the caldera rim. This study uses data from a survey conducted in August 2013 to estimate the total heat flux at the Hot Spot. Total heat flux was predicted to be 130 ± 6 $W \cdot m^{-2}$ based on an estimated 46 ± 2 $W \cdot m^{-2}$ conductive heat flux and an estimated 80 ± 16 $W \cdot m^{-2}$ advective heat flux, for a total heat flow of ~1.1 MW for the 8,600 m^2 vapor-dominated area. This flow is of a similar magnitude as those in other vapor-dominated areas in active volcanic fields and may be sourced by a deeper magma-hydrothermal system rather than local, cooling rock from the last eruption 950 ya. Results of this research add to the current body of knowledge of the Medicine Lake Volcano hydrothermal system and will serve as a baseline should changes to the hydrothermal system occur in the future.

Table of Contents

1. Introduction

The Cascade volcanic arc spans 1,200 km from Lassen Peak in California to Meager Mountain in Canada. It includes over 2,000 distinct Quaternary volcanoes formed due to the subduction of the Juan de Fuca Plate beneath the North American Plate (Fig. 1) (Hildreth, 2007).

Though geologic exploration of the Cascades dates back to the 19th century, thorough geological, geophysical, and geochemical research did not begin until the 1970s (Hildreth, 2007). The 1980 eruption at Mount St. Helens and the desolation it produced served as a wake-up call for the general public about the presence and dangers of volcanoes in the continental United States. In the decades since, the U.S. Geological Survey (USGS) has increased its scientific monitoring efforts throughout the Cascade arc (e.g., Tilling, 1993; Brantley, 1999).

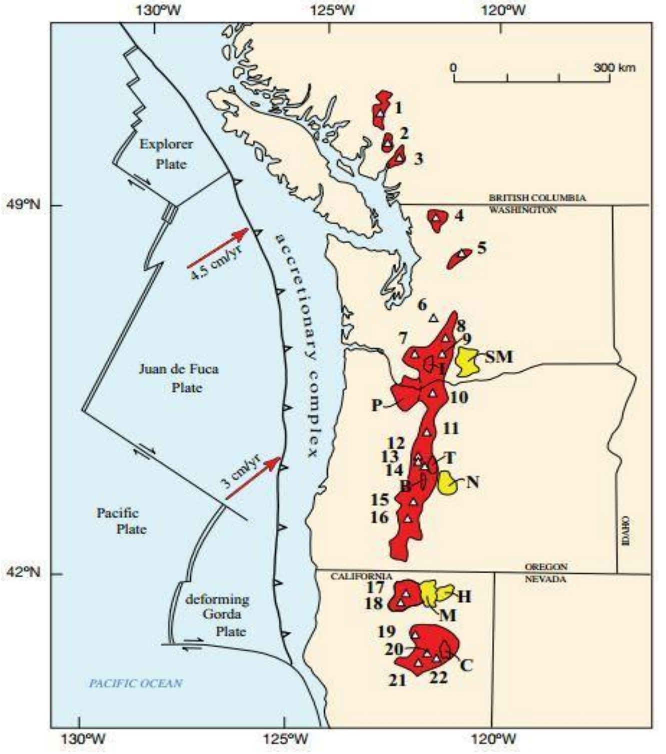

Figure 1. Map showing areas containing Quaternary volcanic vents (red areas) in the Cascade arc. Yellow areas indicate rear arc volcanic fields. Medicine Lake Volcano is labeled as "M." (Hildreth, 2007)

1.1. Hydrothermal Monitoring Efforts in the Cascade Volcanic Arc

Volcano monitoring poses many challenges and forecasting volcanic eruptions is difficult. There are numerous approaches, but the strongest focus is placed on monitoring seismicity and ground deformation due to proven reliability in predicting eruptions (Tilling, 1993).

Other important monitoring involves the study of volcanic hydrothermal systems, which can reveal a wealth of information about associated magma bodies (Hurwitz et al., 2012). There have been multiple recorded instances of chemical changes to magmatically influenced springs and fumaroles during volcanic unrest. Fumarolic areas in particular are likely to exhibit changes due to their close proximity to their magmatic heat sources. For example, elevated carbon dioxide levels have been observed in fumaroles during active periods at Campi Phlegrei caldera in Pozzuoli, Italy (Todesco, 2009).

Historically, campaign-style hydrothermal monitoring efforts have been prompted by other symptoms of volcanic unrest such as increased seismicity or ground deformation (Ingebritsen et al., 2014b). However, without baseline data from the hydrothermal systems under typical conditions, it is difficult to detect abnormalities or changes in the systems.

Concerns over renewed volcanic unrest at South Sister volcano in central Oregon in 2002 led to hydrothermal monitoring by the USGS there and at a few other Cascade sites (Evans et al., 2004). In 2009, this monitoring network was expanded to include a total of 25 different sites at high-risk volcanoes throughout the United States portion of the Cascade arc (Ingebritsen et al., 2014b). These sites include fumarolic areas and magmatically influenced springs and streams (as indicated mainly by He- and C-isotope ratios).

Though methods of collection and data types at individual sites vary, fumarolic sites generally have hourly temperature monitoring and intermittent gas sampling; most stream/spring sites have hourly pressure-temperature-conductivity monitoring and intermittent water sampling and discharge measurements; some stream sites also have hourly temperature monitoring of a nearby source vent, with intermittent gas sampling. Also included in the network are a few sites which lack hourly data, but have had intermittent flux measurements taken by the USGS over several decades. The goal of this study by the USGS is to collect complete baseline data sets for comparison in the event that volcanic activity increases at any of these high-risk sites in the future.

1.2. Medicine Lake Volcano

One of the volcanoes included in this USGS study is Medicine Lake Volcano (MLV) (Fig. 2), a large shield volcano located just east of the main arc, 45 km from the Oregon border in northeastern

California (labeled “M” in Figure 1). Lavas of the volcano cover 7,200 km^2, making it one of the largest volcanoes by area in the entire Cascade arc (Donnelly-Nolan, 2010). The volcano takes its name from the body of water filling part of its 7x12 km caldera (Donnelly-Nolan, 1990).

Figure 2. View of Medicine Lake Volcano from the northeast. (Donnelly-Nolan et al., 2007)

Over the course of its 0.5 Ma history, MLV has erupted hundreds of times with a wide variety of eruptive styles, including at least two explosive events (Donnelly-Nolan et al., 2007). The most recent eruption was 950 ya and consisted of a rhyolite and dacite obsidian flow which formed the distinctive Glass Mountain on the eastern rim of the caldera (e.g., Donnelly-Nolan et al., 2007; Wood and Kienle, 1990). A seismic swarm in the late 1980s, combined with the volcano’s eruptive history, earned it the 12th highest threat ranking among all Cascade volcanoes in the USGS National Volcano Early Warning System (NVEWS) report (Ewert et al., 2005). Despite being ranked as a high-threat volcano by NVEWS, MLV continues to be under-monitored (Donnelly-Nolan et al., 2007).

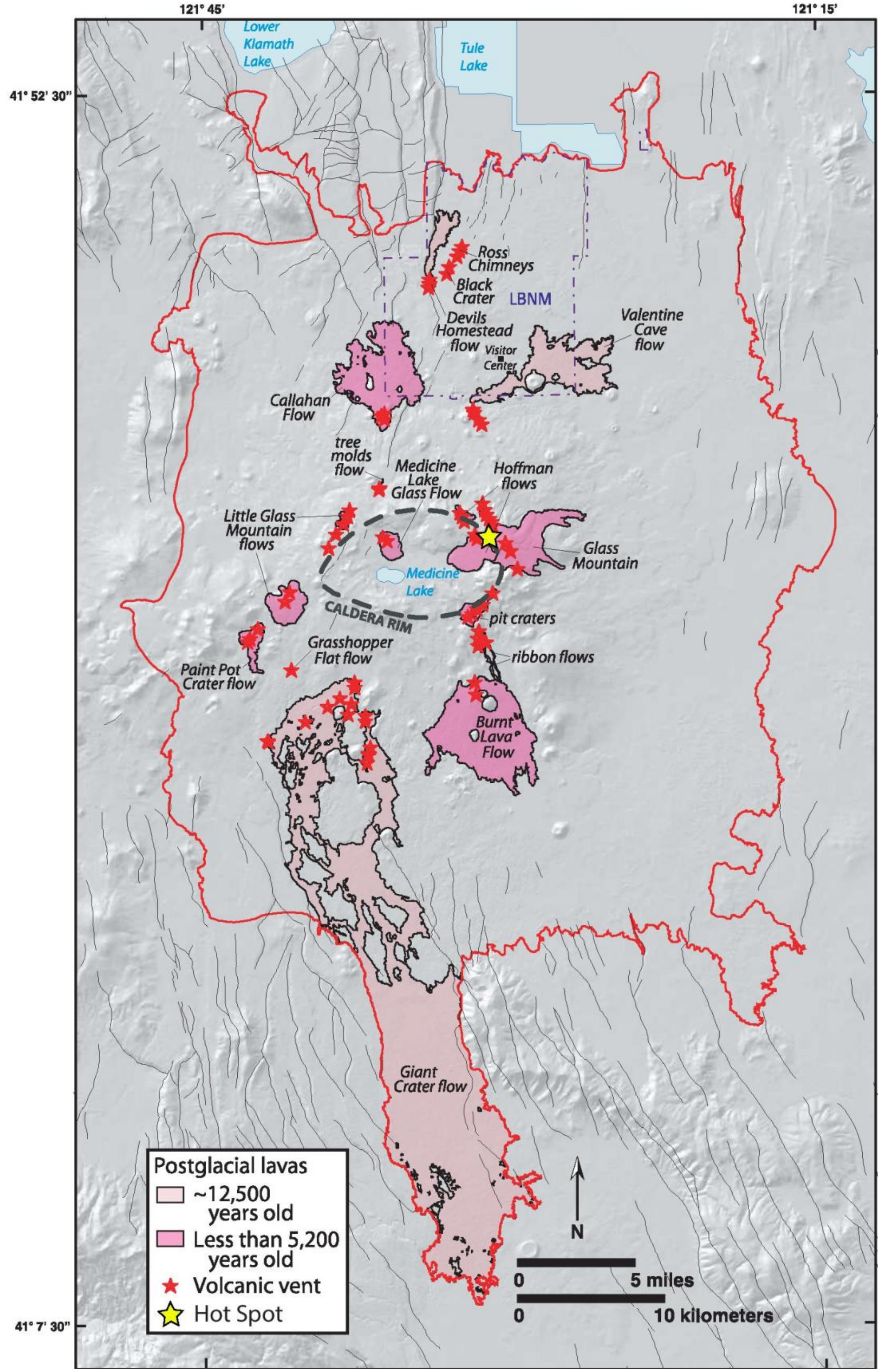

Figure 3. Map showing postglacial lava flows at Medicine Lake volcano by age. Thin black lines are faults. Medicine Lake Volcano is outlined in red. Yellow star indicates the location of the Hot Spot. LBNM is Lava Beds National Monument. (modified from Donnelly-Nolan et al., 2008)

MLV rests at the junction of several major tectonic features including the Walker Lane fault zone to the southeast, the Klamath Graben to the north, and the highland of volcanic vents extending from Mount Shasta to the west (Donnelly-Nolan, 2008). The combined influence of these features leads to crustal extension across the volcano in the east-west direction on northwest to northeast trending faults (e.g., Wood and Kienle, 1990; Hildreth, 2007; Donnelly-Nolan, 2008). A strong correlation between vent location on MLV and faulting has been observed (Donnelly-Nolan, 2008) (Fig. 3).

Seismic studies in the late 20th century indicated the presence of a small, shallow silicic magma body beneath the eastern part of the caldera. These findings are further supported by petrologic studies of the area which indicate crystallization at depths between 3 and 6 km (Donnelly-Nolan et al., 2007).

A shallow, high-temperature hydrothermal system was found while drilling for geothermal energy on the upper part of MLV (Lutz et al., 2000). The only known surficial evidence of this hydrothermal system is a weak fumarole contained within a small area of heated ground on the northwest side of Glass Mountain (e.g., Donnelly-Nolan et al., 2007; Wood and Kienle, 1990). Due to a lack of other hydrothermal features or chemically anomalous springs nearby, this area, referred to as the Hot Spot (Fig. 3), has become the primary hydrothermal-monitoring site at MLV (e.g., Wood and Kienle 1990; Ingebritsen et al., 2014b).

1.3. Medicine Lake Volcano Hot Spot

There are three main types of hydrothermal features found above magma chambers: high-chloride springs, geothermal fumaroles and associated acid-sulfate springs, and volcanic fumaroles (Fig. 4). However, the hydrothermal features at MLV are much more subtle than those depicted in Figure 4, consisting only of the Hot Spot and possibly the slightly thermal Fall River Springs about 60 km south of the Medicine Lake highlands (Mariner and Lowenstern, 1999).

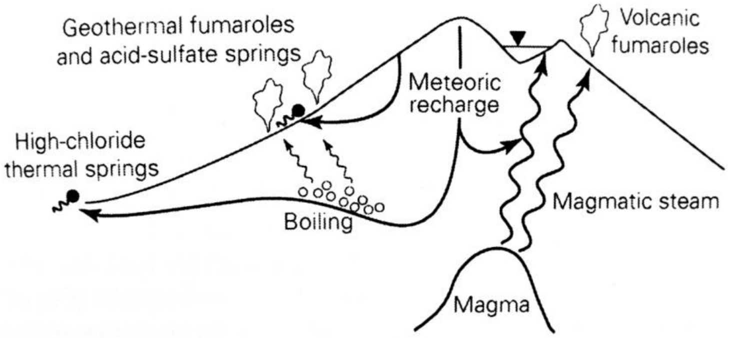

Figure 4. Schematic diagram showing the three primary types ofhydrothermal features. (Ingebritsen et al., 2006)

Robert H. Mariner of the USGS-Menlo Park has hypothesized that the Hot Spot fumarole is geothermal in nature (Mariner, 2008). Geothermal fumaroles, or steam vents, are the result of groundwater being heated to boiling and rising to the surface through faults or cracks as steam (e.g., Ingebritsen et al., 2006). A thick, impermeable cap layer in the form of highly altered volcanic rock prevents MLV's geothermal reservoir from mixing with shallow groundwater (BLM, 1985). Mariner believes that local, residual heat from the eruption that formed Glass Mountain nearly a millennium ago is responsible for the Hot Spot (Mariner, 2008). Alternatively, the Hot Spot could be fed by the deeper magmatic-hydrothermal system through cracks in the cap layer.

In June 2009, a group of researchers from the USGS-Menlo Park facility installed a series of data-logging thermistors at the Hot Spot as a part of the broad Cascade volcano monitoring project described above. Shallow ground temperature data were collected hourly until July 2012. Gas samples were taken at the Hot Spot gas vent once each summer over the course of the three year monitoring period, but most or all of the gas samples were air contaminated (Ingebritsen et al., 2014a). The gas data retrieved from the Hot Spot in this study have yet to be thoroughly analyzed.

A brief ground temperature survey was conducted by the same research team in August 2011. Ground temperature gradients were taken at fourteen different points in the western portion of the hydrothermal area. However, my analysis in summer 2013 showed these data to be insufficient to describe total heat loss from the Hot Spot.

In August 2013, as members of the same USGS-Menlo Park team, Ilana Crankshaw (Carleton College) and I conducted another ground-temperature survey of the Hot Spot to gather more complete data. I have used these data to quantify the heat flow of the MLV Hot Spot.

Results of this research add to the current body of knowledge of the MLV hydrothermal system and will contribute to future monitoring efforts.

2. Field Methods

We took temperature measurements at depths of 0.02, 0.05, 0.1, 0.2, 0.3,...0.8 m at each of 25 points throughout the 8,600 m^2 hydrothermal area (Fig. 5). These points were more broadly distributed than those in the 2011 survey and were predetermined using GPS software to ensure a regular distribution.

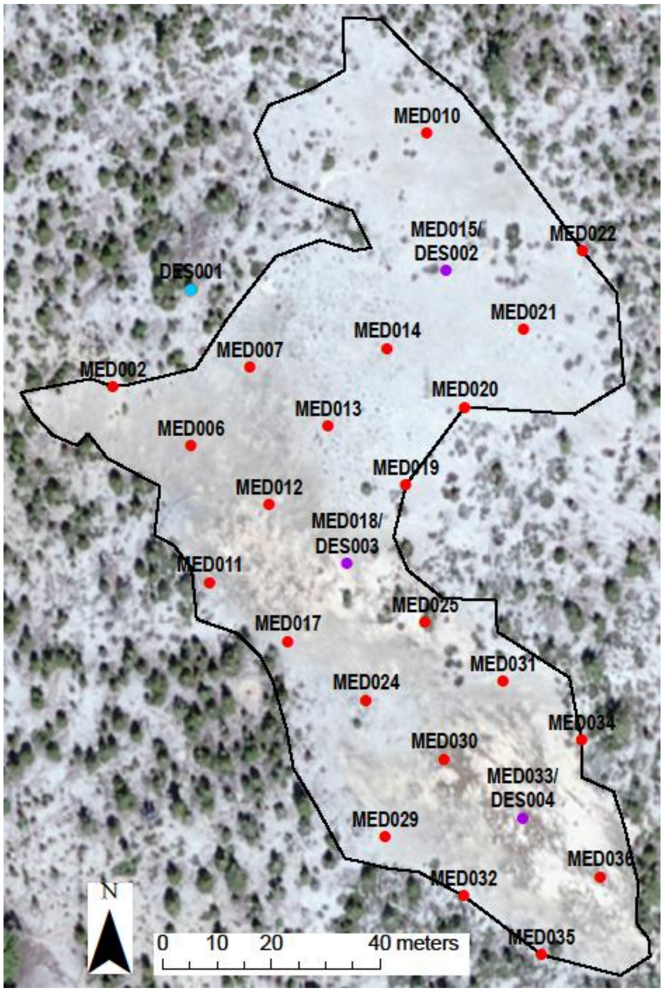

Figure 5. Aerial photograph (Copyright 2014 ESRI) of the Hot Spot with measurement locations indicated by colored circles. Colors correspond with measurement type, with red indicating temperature gradients, blue indicating water vapor mass flux, and purple indicating both. The Hot Spot boundary is outlined in black.

Advective heat transfer caused by vigorous vapor upflow causes some temperature gradients to exhibit strong curvature. The shallower measurements from 0.02 to 0.1 m are important to constrain this curvature and also for assessing near-surface variability.

Measurements at depths ranging from 0.1 to 0.8 m were taken using a meter-long thermistor temperature probe (Fig. 6). Deeper measurements were taken first. We inserted the probe into holes made by hammering a steel rod of similar diameter into the soil. At some locations, we were unable to attain the desired 0.8 m bottom-depth. For measurements at 5 cm and 2 cm, a shorter 10 cm thermistor temperature probe was inserted directly into the soil.

Figure 6. Photograph of equipment used to measure temperature gradients at the Medicine Lake Volcano Hot Spot.

In addition to measuring temperature gradients, we attempted to measure water vapor mass flux from the soil using a new method developed by Hurwitz et al. (2012). Four polyethylene containers were filled with an anhydrite desiccant (Drierite®), covered with a permeable polyester screen, and placed so that the screen touched the soil (Fig. 7). The containers were weighed periodically over an 8-hour period in order to measure absorbed water vapor mass over time. Anhydrite desiccant was chosen because of its ability to absorb 8 wt% water before saturation without absorbing CO_2 (Hurwitz, 2012), which is commonly emitted from the soil in vapor-dominated areas like the Hot Spot.

Figure 7. Photograph of container filled with desiccant used to measure water vapor mass flux at the Medicine Lake Volcano Hot Spot.

3. Analytical Methods

3.1. Conductive Heat Flux

Temperature profiles for each measurement location allow for visual assessment of the data. Based on this assessment, the gradients were grouped into three classes: A, B, and C (Fig. 8). Class A includes all gradients with a bottom-hole temperature of less than 40 °C, all of which exhibit little to no curvature and strong near-surface variability (*e.g.*, near-surface temperature reversals caused by temporal variation in land-surface temperature). Class B includes all gradients with a bottom-hole temperature between 40 and 70 °C, all of which exhibit moderate curvature and moderate near-surface variability. Class C includes all gradients with a bottom-hole temperature greater than 70 °C, all of which exhibit strong curvature and little near-surface variability. Of the 25 measurement locations, 52% were classified as type A, 28% as type B, and 20% as type C.

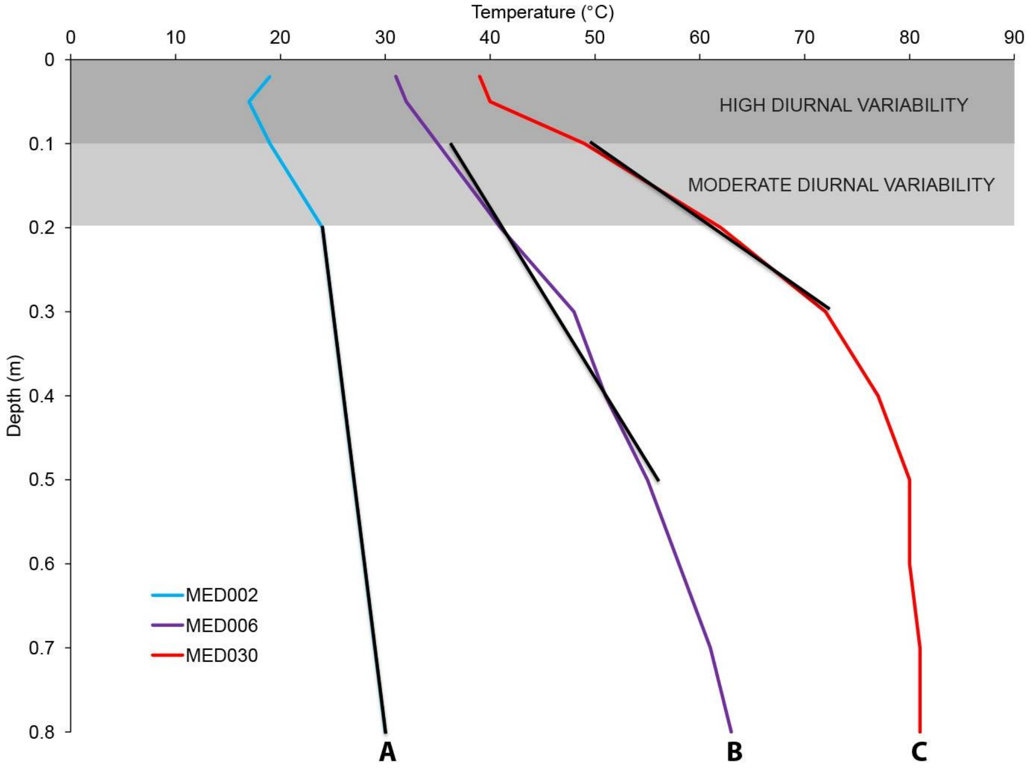

Figure 8. Spaghetti diagram showing selected temperature-depth profiles for each type (labeled A, B, and C). Trendlines fit to each profile are shown in black. Zones of high and moderate "diurnal" variability are indicated in grey; lacking time-series data, here I use "diurnal" as shorthand to denote effects of temporal variation in land-surface temperature. Note that the amount of near-surface variation declines with increased bottom-hole temperature.

Based on methods used by Hurwitz et al. (2012), I chose the most linear portions of the profiles within each class and applied a trendline. For class A sites, I applied the trendline to measurements of depths from 0.2 to 0.8 m, from 0.1 to 0.5 m for class B sites, and from 0.1 to 0.3 for class C sites (Fig. 8). For one location, MED035, I removed the temperature measurement at 0.5 m when determining the trendline because it appeared to be the result of probe malfunction.

A majority of the temperature-depth profiles show a systematic increase in temperature with depth. A few, however, had more erratic behavior with recorded temperature occasionally dropping, sometimes dramatically, with depth. Even in these cases, though, the general trend was positive. The most erratic curves correspond with late-day measurements, suggesting that the probe was malfunctioning toward the end of the measurement period.

The temperature gradients determined as described above and illustrated in Figure 8 were used to estimate conductive heat flux using Fourier's law of heat conduction:

$$Q_{cond} = K\left(\frac{\Delta T}{\Delta z}\right) \tag{1}$$

where K (W·m^{-1}K^{-1}) is the bulk thermal conductivity, T is temperature, and z is depth. A value of 1.3 W·m^{-1}K^{-1} was used for thermal conductivity based on calculations made for similar soil material at hydrothermal areas in the Yellowstone Plateau Volcanic Field (Hurwitz et al., 2012).

3.2. Advective Heat Flux

3.2.1. Desiccant Experiment

It gradually became clear during data collection that the scale used to weigh the desiccant containers was malfunctioning under field conditions. However, data from all four locations show a general trend of increasing mass. In an attempt to correct for the error in individual measurements, the cumulative weight of each container was plotted over time and a linear trendline was applied which assumed that the initial weights were accurate. Trendlines fitted to the field data exhibited poor (R^2 <

0.2) to moderate ($0.7 \geq R^2 \geq 0.8$) fit (Fig. 9). The slope of each trendline was used to determine the water vapor flux for each location.

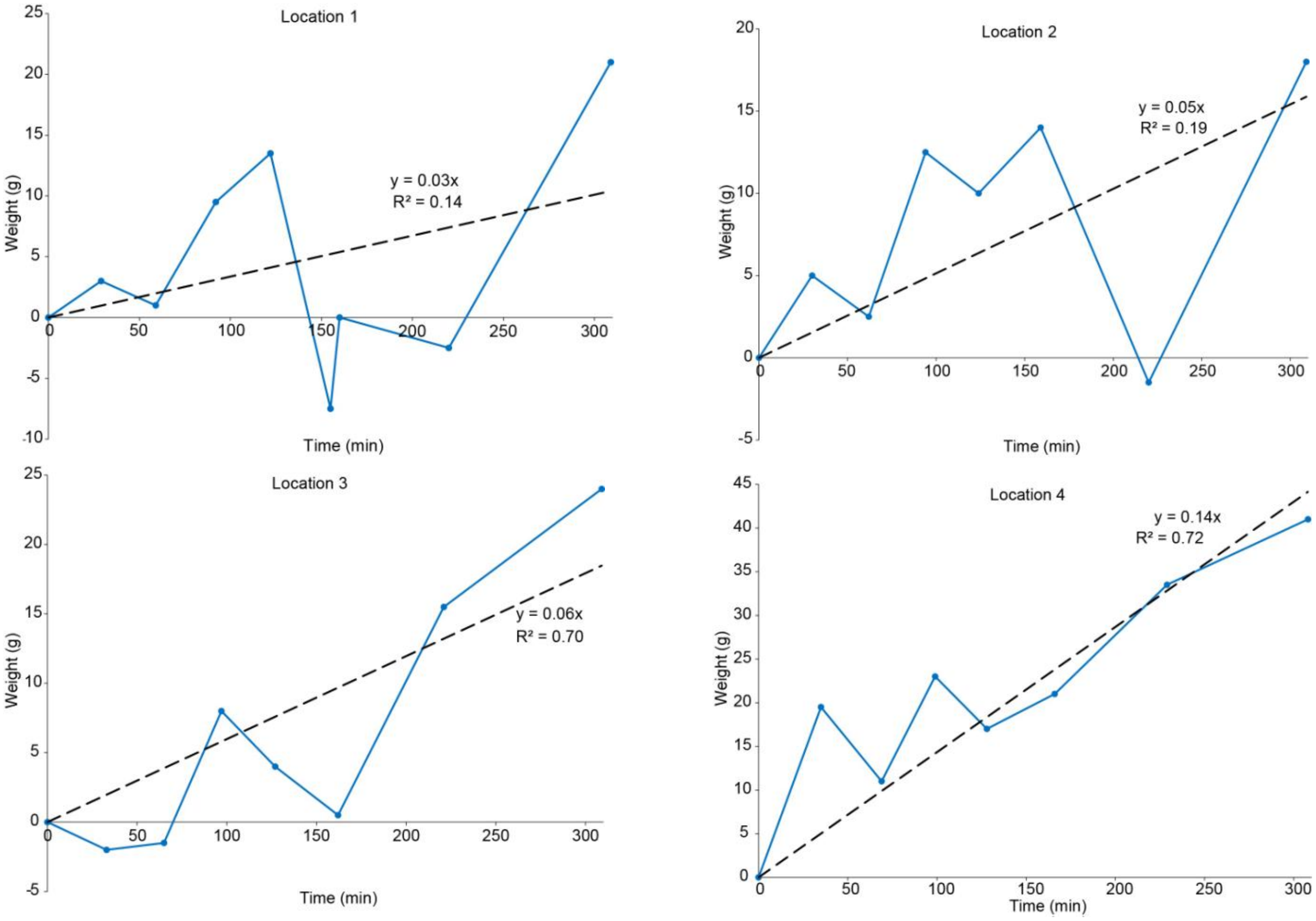

Figure 9. Plots of cumulative water vapor weight over time for the 4 desiccant container locations. Fitted trendlines (black dashed-lines) are labeled with their corresponding equations and R^2 values.

These trendlines ($\Delta m/\Delta t$) (Fig. 9) were used to determine the advective heat flux (Q_{adv}) at each location through the equation

$$Q_{adv} = h\left(\frac{\frac{\Delta m}{\Delta t}}{A}\right) \tag{2}$$

where h is the vapor enthalpy (2,676 kJ-kg^{-1}), $\Delta m/\Delta t$ (g/s) is the time-dependent mass of water absorbed by the desiccant and A (m^2) is the area of the container in contact with the ground (Hurwitz et al., 2012; note that I correct their Eq. 18 by using enthalpy rather than latent heat).

3.2.2.Bredehoeft and Papadopulos Model

Bredehoeft and Papadopulos (1965) developed a type-curve method to determine rates of one-dimensional groundwater flow. Ingebritsen et al. (2006) describe a version of the Bredehoeft and Papadopulos method that allows for its application in estimating advective heat flux based on the degree of curvature of temperature profiles.

In order to apply this method to my data, each temperature gradient was plotted on a log scale versus a linear scale for depth and evaluated for linearity (Nathenson et al., in review). Only those gradients with a linear trendline with an R^2 greater than 0.7 were modeled with the Bredehoeft and Papadopulos (1965) method.

Type-curves were developed using the equation:

$$f\left(\beta, \frac{z}{L}\right) = \frac{\left[exp\left(\frac{\beta z}{L}\right) - 1\right]}{\left[exp(\beta) - 1\right]} \tag{3}$$

$$\beta = \frac{c_v \rho_v q_v L}{K} \tag{4}$$

where z is the intermediate depth, L is the distance between the constant temperature boundaries, and β is a dimensionless parameter (a Peclet number) ranging from 0 to 30 and is negative for upflow; c_v is the heat capacity of water vapor, ρ_v is the density of water vapor, q_w is the volumetric flux of water vapor, and K is the thermal conductivity of the soil.

In order to plot the field data over the type-curves, the equation

$$f\left(\beta, \frac{z}{L}\right) = \frac{(T_z - T_U)}{(T_L - T_U)} \tag{5}$$

was used, where T_U, T_L, and T_z are the measured temperatures at the upper and lower boundaries and at an intermediate depth, respectively. Only the sections of the gradients from 0.1 to 0.8 m were used, with 0.02 m representing the surface temperature in order to minimize the effect of near-surface variability. For the location MED035, a linear trendline was applied to determine the gradient in order to correct for erratic temperature measurements (Fig. 10).

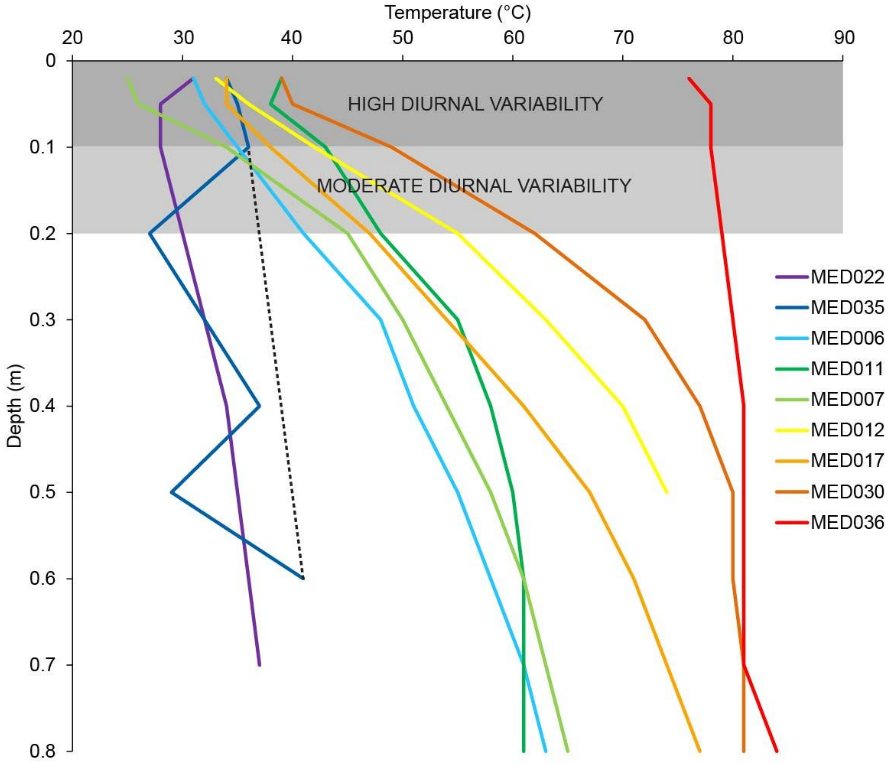

Figure 10. Spaghetti diagram showing temperature-depth profiles used in the Bredehoeft and Papadopulos (1965) model. Line colors correspond with bottom-hole temperature ranging from coldest (purple) to hottest (red). Black dotted-line represents corrected profile for MED035. "Diurnal" denotes effects of temporal variation in land-surface temperature. Note that the amount of near-surface variation declines with increased bottom-hole temperature.

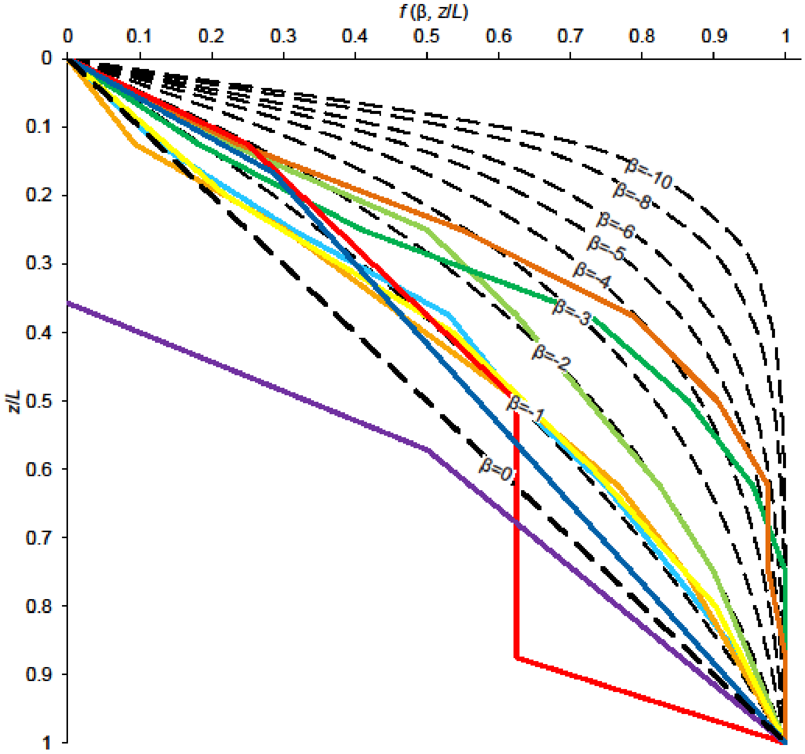

Figure 11. Temperature profiles from Figure 10 superimposed on type curves (black dashed-lines) derived from the Bredehoeft and Papadopulos (1965) equation. Corresponding β values are labeled.

The volumetric flux of water vapor velocity was determined by using type curves to estimate β values (Fig. 11) and modifying Equation 5 of Bredehoeft and Papadopulos (1965) to reflect water-vapor (rather than liquid) properties:

$$q_v = \frac{\beta K}{c_v \rho_v L} \tag{6}$$

And volumetric flux was converted to advective heat flux using the equation

$$Q_{adv} = q_v \rho_v h \tag{7}$$

3.3. GIS

The total conductive and advective heat fluxes for the Hot Spot were estimated from raster surfaces interpolated using ArcGIS 10.1. The conductive heat flux raster was made using Empirical Bayesian Kriging, a geostatistical interpolation method that uses repeated simulations to minimize estimation error. This method could not be used with the water vapor mass flux data due to the small sample size of the desiccant experiment, so Ordinary Kriging was applied instead. Advective heat flux estimates based on the Bredehoeft and Papadopulos model proved problematic to interpret and thus were not converted into a raster and not used in the estimated total heat flux. The Hot Spot boundary for the rasters (Fig. 5) was determined from GPS measurements taken during the 2011 survey of the area and is based on the apparent tree line.

3.4. Total Heat Flux

Finally, estimates of total heat flux of the hydrothermal area were calculated by applying the equation

$$Q_{total} = Q_{cond} + Q_{adv} \tag{8}$$

to the conductive heat flux raster and each of the advective heat flux rasters in ArcGIS.

4. Results

4.1. Conductive Heat Flux

The mean conductive heat flux calculated from the raster is 46 ± 2 $W \cdot m^{-2}$. The maximum predicted value is 64 $W \cdot m^{-2}$ and the minimum is 28 $W \cdot m^{-2}$. A summary of heat flux calculations and trendline fits by curve type can be found in Table 1. The west-central portion of the hydrothermal area exhibited the highest conductive heat flux, with the northeast and southeast portions exhibiting the lowest fluxes (Fig. 12).

Table 1. Conductive heat flux results by gradient type

Gradient type	Count	Mean R^2 of trend	Mean Temperature Gradient	Mean Q_{cond} ($W \cdot m^{-2}$)
A	13	0.96	19	25 ± 2.8
B	7	0.97	44	58 ± 5.3
C	5	0.99	61	80 ± 23

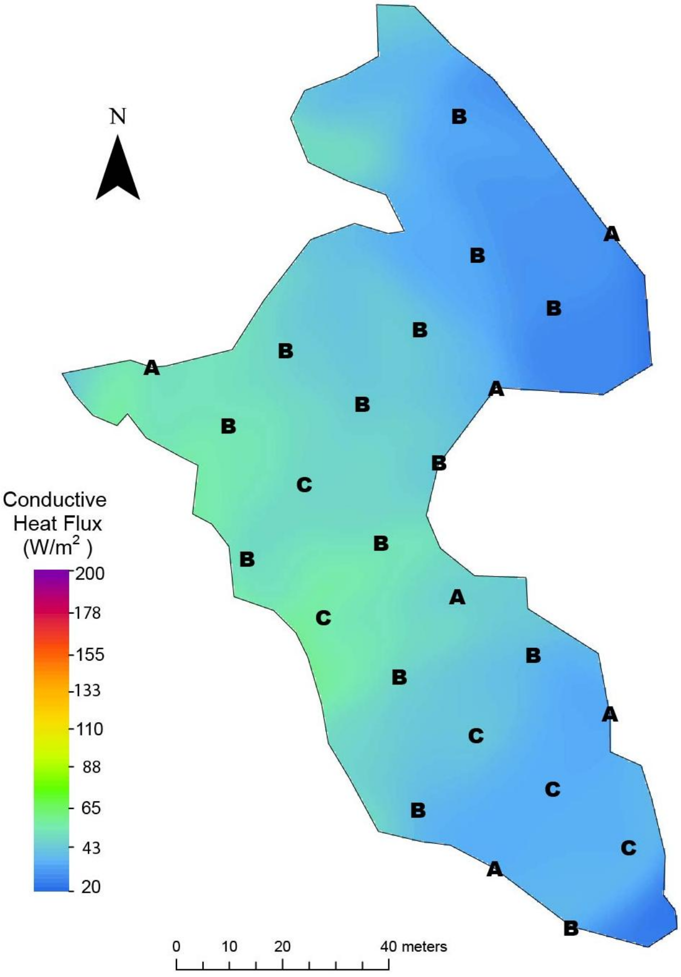

Figure 12. Map showing predicted conductive heat flux distribution across the Hot Spot. Letters indicate temperature-depth measurement locations and correspond with bottom-hole temperature, as defined in section 3.1.

4.2. Advective Heat Flux

4.2.1. Desiccant Experiment

The mean advective heat flux determined using the desiccant-chamber method is 80 ± 16 W·m^{-2}. A summary of advective heat flux calculations and trendline fits can be found in Table 2. Similar to the conductive heat flux, advective heat flux was found to be highest (a maximum of 150 W·m^{-2}) in the southeast portion of the hydrothermal area and lowest (a minimum of 41 W·m^{-2}) in the northwest portion (Fig. 13).

Table 2. Advective heat flux results by measurement site

Site	R^2	Q_{adv} (W·m^{-2})
DES001	0.14	40.0
DES002	0.19	54.6
DES003	0.70	63.5
DES004	0.72	152

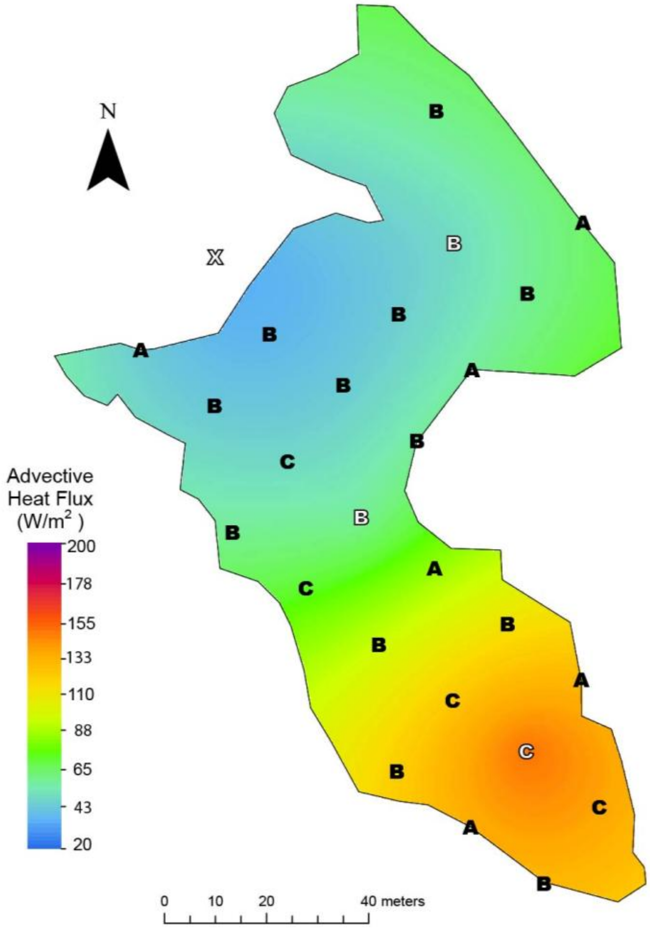

Figure 13. Map showing predicted advective heat flux distribution (based on desiccant measurements) across the Hot Spot. White letters indicate desiccant measurement locations; black letters are temperature-depth-only locations (as in Fig. 12). "X" is a desiccant-only location.

4.2.2.Bredehoeft and Papadopulos Model

The advective flux calculated using the Bredehoeft and Papadopulos model ranged from 0 W·m^{-2} to 6500 W·m^{-2} with and mean flux of 3600 ± 830 W·m^{-2} (Table 3).

Table 3. Summary of advective heat flux and corresponding β values from the Bredehoeft and Papadopulos model by site

Site	Gradient type	Model fit (R^2)	Q_{adv} (W·m^{-2})	β
MED006	B	0.71	2200	-1
MED007	B	0.72	4400	-2
MED011	B	0.73	6500	-3
MED012	C	0.93	2200	-1
MED017	C	0.95	6500	-3
MED022	A	0.77	0	0
MED030	C	0.99	6500	-3
MED035	B	0.89	1500	-0.5
MED036	C	0.90	2200	-1

5. Discussion

5.1. Total Heat Flux

The total heat flux was not calculated using the predicted advective heat flux values from the Bredehoeft and Papadopulos (1965) model due to their unreasonably high values; rather it was calculated as the sum of the conductive heat-flux values and desiccant-based estimates of advective heat flux. This applicability of the Bredehoeft and Papadopulos model is further addressed below.

Total estimated heat flux of the MLV Hot Spot is 130 ± 6 W·m^{-2}. This value is similar to estimated heat fluxes at other vapor-dominated areas in active volcanic fields including ~130 W·m^{-2} at the Yellowstone Plateau (Hurwitz et al., 2012). A summary of all results by measurement site can be found in Table 4.

The spatial distribution of the total heat flux closely mimics trends seen in the predicted advective heat flux, with the highest fluxes in the southeast portion of the Hot Spot and the lowest fluxes in the northeast portion (Fig. 14). Apparent extension of high heat fluxes outside of the Hot Spot boundary is likely the result of the desiccant experiment's small sample size. However, since the boundary used in this analysis is based on a qualitative field survey, future work at the MLV Hot Spot could use temperature measurements to better constrain its true area.

Table 4. Summary of all results by measurement site

Site	Easting	Northing	BHT[a] (°C)	T Grad.[b] (°C·m^{-1})	β	Q_{adv} B&P[c] (W·m^{-2})	Vapor flux (kg·s^{-1}·m^{-2})	Q_{adv} Desiccant (W·m^{-2})	Q_{cond} (W·m^{-2})	Q_{total} (W·m^{-2})
DES001	622998.9	4607060	-	-	-	-	2.6×10^{-8}	40.0	-	-
MED002	622984.5	4607042	30	10	-	-	-	-	13	-
MED006	622998.9	4607031	63	51	-1	2300	-	-	67	-
MED007	623009.7	4607045	65	61	-2	4600	-	-	79	-
MED010	623042.3	4607089	63	39	-	-	-	-	50	-
MED011	623002.4	4607006	61	46	-3	6800	-	-	60	-
MED012	623013.2	4607020	74*	75	-1	2300	-	-	98	-
MED013	623024.1	4607035	46	22	-	-	-	-	28	-
MED014	623034.9	4607049	55	44	-	-	-	-	57	-
MED015/ DES002	623045.8	4607063	43*	27	-	-	3.6×10^{-8}	54.6	35	82
MED017	623016.8	4606995	77	67	-3	6800	-	-	87	-
MED018/ DES003	623027.6	4607009	61	44	-	-	4.2×10^{-8}	63.5	58	110
MED019	623038.5	4607024	51	26	-	-	-	-	33	-
MED020	623049.3	4607038	40	15	-	-	-	-	20	-
MED021	623060.1	4607053	44	22	-	-	-	-	29	-
MED022	623071	4607067	37*	14	0	0	-	-	18	-
MED024	623031.1	4606984	47	24	-	-	-	-	31	-
MED025	623042	4606999	40	22	-	-	-	-	29	-
MED029	623034.6	4606959	43	15	-	-	-	-	19	-
MED030	623045.5	4606973	81	120	-3	6800	-	-	150	-
MED031	623056.3	4606988	46	23	-	-	-	-	30	-
MED032	623049	4606948	34	9.1	-	-	-	-	12	-
MED033/ DES004	623059.9	4606963	81	37	-	-	1.0×10^{-7}	152	48	180
MED034	623070.7	4606977	32	11	-	-	-	-	15	-
MED035	623063.4	4606937	41*[d]	37	-0.5	1500	-	-	48	-
MED036	623074.2	4606952	84	10	-1	2300	-	-	13	-
[e]Mean	-	-	54	35	-	3700	5.1×10^{-8}	77.6	45	120

[a] Bottom-hole temperature

[b] Temperature gradient

[c] Bredehoeft and Papadopulos

[d] Trendline applied to gradient

[e] Means not derived from geostatistical analysis

*failed before 0.8 m depth

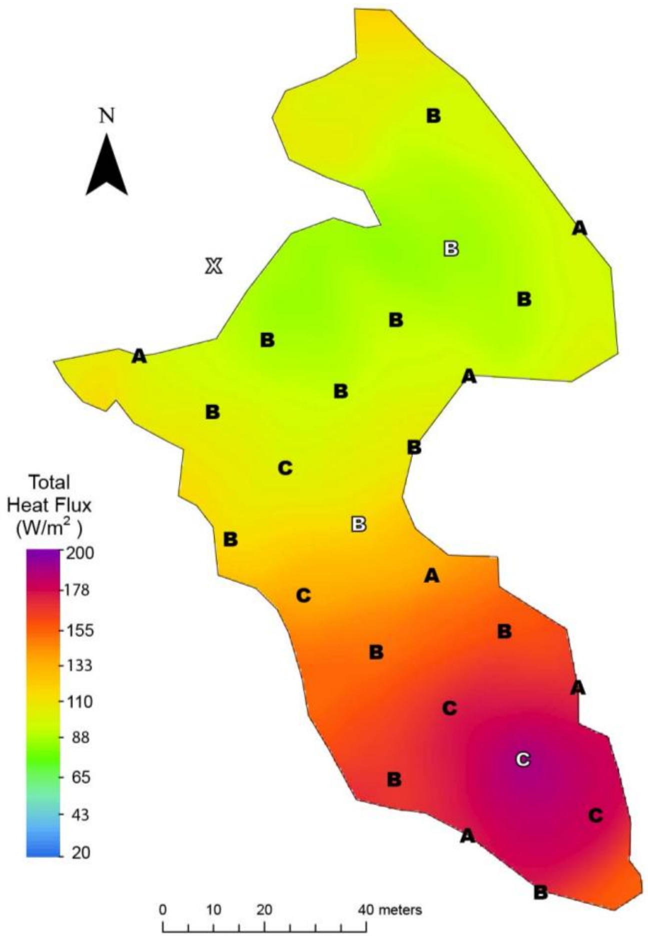

Figure 14. Map showing predicted total heat flux distribution across the Hot Spot. Letters indicate measurement locations. Black lettering indicates temperature-depth-only locations; those with white lettering also have desiccant measurements. Letters A – C correspond with bottom-hole temperature ranges as described in section 3.1. "X" is a desiccant-only location.

5.2. Conductive Heat Flux

The estimated conductive heat flux throughout the Hot Spot varies from 27-64 W·m^{-2}, whereas the regional conductive heat flux is about 0.1 W·m^2 (Ingebritsen and Mariner, 2010). This huge heat-flow excess relative to regional values is consistent with delivery of heat by hydrothermal circulation.

The shapes of the curves for the three temperature-profile types (A, B, and C) are related to the amount of advective heat flow at each location (Hurwitz et al., 2012). Higher levels of advective heat flow lead to the strong curvature observed in the type C class. This curvature corresponds with higher temperatures because more advective heat transfer means more heat in general. The type B and C gradients are not as strongly affected by temporal variability at the land surface because vigorous upflow of heat in these areas overwhelms the land-surface boundary effects.

5.3. Desiccant Experiment

Similar to the conductive heat flux, advective heat flux was found to be highest in the southeast portion of the hydrothermal area and lowest in the northwest portion, though the range of advective heat fluxes is significantly larger (41 to 150 $W \cdot m^{-2}$) (Fig. 13). Unfortunately, due to the small sample size (4), and equipment malfunction leading to irregular measurements, the precision of these results is relatively poor. However, the results appear reasonable in light of the good agreement between predicted total advective heat flux of the Medicine Lake Hot Spot and advective heat flux calculations for similar vapor-dominated hydrothermal areas at other volcanoes, such as ~95 $W \cdot m^{-2}$ on the Yellowstone Plateau (Hurwitz et al., 2012).

5.4. Bredehoeft and Papadopulos Model and Depth to Water Table

The application of the Bredehoeft and Papadopulos (1965) approach to this problem is not as straightforward as initially hoped. Of the 9 locations that passed the trendline test, 8% are curve type A, 58% are type B, and 33% are type C. This distribution is strongly skewed toward the higher temperature types B and C compared to the total distribution of all data (52 % type A, per Table 5).

Table 5. Distribution of gradient types among all gradients compared to gradients used in the Bredehoeft and Papadopulos model for advective heat flux

Gradient type	All gradients	B&P[a] model
A	52%	8%
B	28%	58%
C	20%	33%

[a] Bredehoeft and Papadopulos

Thus hotter temperature-depth profiles are disproportionately represented in the model. Nonetheless the predicted fluxes are impossibly high (60x greater than the values predicted through by desiccant experiment). The Bredehoeft and Papadopulos approach was developed for liquid groundwater and thus assumes a constant density. Applying the equation to a vapor-dominated area like the Hot Spot violates this assumption because steam is highly compressible. Further, the Bredehoeft and Papadopulos approach has no provision for vaporization and condensation (latent heat), which are also likely important in this environment. However, it seems unlikely that such issues would lead to a 60-fold discrepancy.

A more likely explanation relates to the value used for the parameter *L*, the distance between the constant temperature boundaries that are assumed in Bredehoeft and Papadopulos. The value that I used in the model was arbitrarily taken to be the same as the deepest temperature measurements taken, 0.8 m. The depth to an underlying, boiling water table might better represent the physics assumed by Bredehoeft and Papadopulos. By taking the ratio of advective heat flux estimated using the Bredehoeft and Papadopulos model to the flux estimated using the desiccant, the depth to the water table can be estimated to be around 60x larger than the current *L* value, or approximately 50 m. This depth is reasonable when compared to the elevation of Medicine Lake, which is ~100 m lower and 6 km away.

Results from the Bredehoeft and Papadopulos approach can also serve as a qualitative index of the relative importance of advective heat flow across the Hot Spot. The dimensionless parameter β in the Bredehoeft and Papadopulos equation is a form of the Peclet number, *Pe*, which is a measure of the relative importance of advective heat transport (Ingebritsen, 2006). A *Pe* value of 0 indicates heat transport entirely by conduction (no advection). Table 3 summarizes the findings of the Bredehoeft and Papadopulos model, including the β associated with each profile. Geographic distribution of β values aligns with the predicted advective heat flux based on the desiccant experiment. Profiles with higher β values were located in the southeast portion of the hydrothermal area, and those with the lower β values were generally located in the northeast portion. Higher β values generally correspond with higher bottom-hole temperatures (Table 3), with the major exception of MED036. Despite having the highest recorded bottom-hole temperature, it is assigned a relatively low β value of -1. Rather than exhibiting the convex-upward shape typical of highly advective heat flow (as in the MED030 and MED012 profiles), MED036 remains around 80 °C all the way to the surface. Such behavior is indicative of extremely high advective heat flow, but due to the Bredehoeft and Papadopulos model's reliance on profile curvature, it is not recognized as such by the model.

5.5. Inferring Carbon Dioxide Concentration

The nearly isothermal sections toward the bottom of several of the type C temperature-depth profiles (Fig. 10) suggest that temperatures are near the local boiling point (Hurwitz, 2012). The pure-water boiling point at the Hot Spot, based on elevation and the typical barometric pressure observed by the nearby weather station is ~93 °C. However, the curvature of the temperature profiles suggests the possibility of boiling at temperatures ~81 °C. This discrepancy is common in hydrothermal areas and may be accounted for by the presence of volatile solutes in the water, increasing the vapor pressure and depressing the boiling point (Lowenstern, 2001). In the case of magmatically influenced areas like the Hot Spot, CO_2 is the likely culprit (Hurwitz, 2012). It may be possible to estimate CO_2 levels in the water vapor the boiling point depression. Such an estimate would be particularly useful in this instance, because gas sampling at the Hot Spot by the USGS over the years has been generally unsuccessful. High levels of N_2 in the samples indicate that they were contaminated with atmospheric gas prior to reaching the surface.

6. Conclusions

Total heat flux at the MLV Hot Spot (~130 $W \cdot m^{-2}$, ~1.1 MW total) is of a similar magnitude as other vapor-dominated areas in active volcanic fields and may be sourced by a deeper magma-hydrothermal system rather than local, cooling rock from the last eruption 950 ya. The vapor may originate from a boiling water table at ~50 m depth.

Malfunctioning equipment and a small sample size compromise the accuracy of these results to an unknown extent. Further work on heat flow at the Hot Spot should focus on attaining more reliable advective heat flux measurements, either through an expanded field survey and / or by resolving the Bredehoeft and Papadopulos model as applied to vapor-dominated areas with no well-defined lower boundary condition.

This study has helped advance the understanding of the MLV hydrothermal system and will serve as a baseline study for future changes at the Hot Spot.

7. Acknowledgements

This research was funded by the U.S. Geological Survey (USGS) as a part of its monitoring efforts for the Cascade volcanic arc. I would like to thank my USGS research advisor Steve Ingebritsen, my academic advisor Zeb Page, as well as Steve Wojtal, Ilana Crankshaw, Shaul Hurwitz, Dave Stonestrom, Bill Evans, Julie Donnelly-Nolan, and my family for all of their support and guidance throughout this process.

8. References

Bargar, K.E., and Keith, T.E.C., 1997, Estimated temperatures for geothermal drill holes at Medicine Lake Volcano, northeastern California, based on fluid inclusion and hydrothermal mineralogy studies: U.S. Geological Survey Open-File Report 97-716.

BLM, USFS, SCAPCD, and BPA, 1999, Telephone Flat geothermal development project environmental impact statement and environmental impact report, California State Clearinghouse number 97052078.

Brantley, S.R., 1999, Volcanoes of the United States: U.S. Geological Survey General Interest Publication, v. 1.1.

Bredehoeft, J.D., and Papadopulos, I.S., 1965, Rates of Vertical Groundwater Movement Estimated from the Earth's Thermal Profile: Water Resources Research, v. 1, p. 325–328.

Donnelly-Nolan, J.M., 2010, Geologic map of Medicine Lake volcano, northern California: U.S. Geological Survey Scientific Investigations Map 2927, scale 1:50,000.

Donnelly-Nolan, J.M., Grove, T.L., Lanphere, M. a., Champion, D.E., and Ramsey, D.W., 2008, Eruptive history and tectonic setting of Medicine Lake Volcano, a large rear-arc volcano in the southern Cascades: Journal of Volcanology and Geothermal Research, v. 177, p. 313–328, doi: 10.1016/j.jvolgeores.2008.04.023.

Donnelly-Nolan, J.M., Nathenson, M., Champion, D.E., Ramsey, D.W., Lowenstern, J.B., and Ewert, J.W., 2007, Volcanic hazard assessment for Medicine Lake volcano, northern California: U.S. Geological Survey Scientific Investigations Report 2007-5174-A, p. 26.

Donnelly-Nolan, J.M., 1990, Geology of Medicine Lake volcano, California Cascade Range: Transactions of the Geothermal Resources Council, v. 14, part 2, p. 1,395-1,396.

Donnelly-Nolan, J.M., Champion, D.E., Miller, C.D., Grove, T.L., and Trimble, D.A., 1990, Post-11,000-year volcanism at Medicine Lake volcano, Cascade Range, northern California: Journal of Geophysical Research, v. 95, p. 19,693-19,704.

Evans, W.C., van Soest, M.C., Mariner, R.H., Hurwitz, S., Ingebritsen, S.E., Wicks, C.W., Jr., and Schmidt, M.E., 2004, Magmatic intrusion west of Three Sisters, central Oregon, USA: The perspective from spring geochemistry: Geology, v. 32, p. 69-72.

Ewert, J.W., Guffanti, M., and Murray, T.L., 2005, An assessment of volcanic threat and monitoring capabilities in the United States: Framework for a National Volcanic Early Warning System: U.S. Geological Survey Open-File Report 2005-1164, p. 62.

Hildreth, Wes, 2007, Quaternary magmatism in the Cascades; geologic perspectives: U.S. Geological Survey Professional Paper 1744, p. 125, [http://pubs.usgs.gov/pp/pp1744/].

Hurwitz, S., Harris, R.N., Werner, C.A., and Murphy, F, 2012, Heat flow in vapor dominated areas of the Yellowstone Plateau Volcanic Field: Implications for the thermal budget of the Yellowstone Caldera, *J. Geophys. Res., 117*, B10207, doi: 10.1029/2012JB009463.

Ingebritsen, S.E., Galloway, D.L., Colvard, E.M., Sorey, M.L., and Mariner, R.H., 2001, Time variation of hydrothermal discharge at selected sites in the western United States: Implications for monitoring: Journal of Volcanology and Geothermal Research, v. 111, p.1-23.

Ingebritsen S.E., Gelwick, K.D., Randolph-Flagg, N.G., Crankshaw, I.M., Lundstrom, E.A., McCulloch, C.L., Murveit, A.M., Newman, A.C., Mariner, R.H., Bergfeld, D., Tucker, D.S., Schmidt, M.E., Spicer, K.R., Mosbrucker, A.R., and Evans, W.C., 2014a, Hydrothermal monitoring data from the Cascade Range, northwestern United States, doi:10.5066/F72N5088.

Ingebritsen, S.E., and Mariner, R.H., 2010, Hydrothermal heat discharge in the Cascade Range, northwestern United States: Journal of Volcanology and Geothermal Research, v. 196, p. 208–218, doi: 10.1016/j.jvolgeores.2010.07.023.

Ingebritsen, S.E., Randolph-Flagg, N.G., Gelwick, K.D., Lundstrom, E.A., Crankshaw, I.M., Murveit, A.M., Schmidt, M.E., Bergfeld, D., Spicer, K.R., Tucker, D.S., Mariner, R.H., and Evans, W.C., 2014b, Hydrothermal monitoring in a quiescent volcanic arc: Cascade Range, northwestern United States: Geofluids, doi: 10.1111/gfl.12079.

Ingebritsen, S.E., Sanford, W., and Neuzil, C., 2006, Groundwater in Geologic Processes: Cambridge University Press, 2nd ed.

Lowenstern, J.B., 2001, Carbon dioxide in magmas and implications for hydrothermal systems: Mineral Deposita,, p. 490–502, doi: 10.1007/s001260100185.

Lutz, S.J, Hulen, J.B., and Schriener Jr., A., 2000, Alteration, geothermometry, and granitoid intrusions in well GMF 31-17, Medicine Lake Volcano geothermal system, California, *in* Proceeds of the twenty-fifth workshop on geothermal reservoir engineering, Stanford University, California.

Mariner, Pers. Comm. with S.E. Ingebritsen, 16 May 2008.

Mariner, R.H., and Lowenstern, J.B., 1999, The geochemistry of waters from springs, wells and snowpack on and adjacent to Medicine Lake volcano, northern California: Transactions Geothermal Resources Council, v. 23, p. 319-326.

Nathenson, M., Urban, T.C., Covington, H.R., in review, Geologic and geophysical data for wells drilled at Raft River Valley, Cassia County, Idaho, in 1977-1978 and data for wells drilled previously: U.S. Geological Survey Open-File Report XXXX-XXXX.

Tilling, R.I., 1993, Monitoring Active Volcanoes: U.S. Geological Survey General Interest Publication. [http://pubs.usgs.gov/gip/monitor/techniques.html].

Todesco, M., 2009, Signals from the Campi Flegrei hydrothermal system: Role of a “magmatic” source of fluids, J. Geophys. Res., 114, B05201, doi: 10.1029/2008JB006134.

Wood and Kienle, 1990, Volcanoes of North America: United States and Canada: Cambridge University Press, p. 354, 212-214.

Appendix A. Raw temperature-depth measurements

Site	Easting	Northing	Temperature (°C)									
	(WGS84/NAD83 Z10T)		0.02	0.05	0.1	0.2	0.3	0.4	0.5	0.6	0.7	0.8
MED002	622984.5	4607042	19	17	19	24	25	26	27	28	29	30
MED006	622998.9	4607031	31	32	35	41	48	51	55	58	61	63
MED007	623009.7	4607045	25	26	34	45	50	54	58	61	63	65
MED010	623042.3	4607089	37	37	38	41	44	49	53	58	61	63
MED011	623002.4	4607006	39	38	43	48	55	58	60	61	61	61
MED012	623013.2	4607020	33	36	42	55	63	70	74	FAIL	FAIL	FAIL
MED013	623024.1	4607035	31	30	30	33	37	39	41	43	45	46
MED014	623034.9	4607049	27	27	31	37	41	44	49	52	53	55
MED015	623045.8	4607063	32	28	30	32	35	37	40	43	FAIL	FAIL
MED017	623016.8	4606995	34	34	38	47	54	61	67	71	74	77
MED018	623027.6	4607009	34	34	36	39	44	49	53	56	59	61
MED019	623038.5	4607024	36	36	35	35	38	41	44	46	49	51
MED020	623049.3	4607038	34	31	30	31	33	35	36	38	39	40
MED021	623060.1	4607053	32	29	29	31	34	37	39	41	43	44
MED022	623071	4607067	31	28	28	30	32	34	35	36	37	FAIL
MED024	623031.1	4606984	39	37	32	33	37	39	41	44	46	47
MED025	623042	4606999	28	28	28	30	34	37	39	41	42	40
MED029	623034.6	4606959	38	36	34	35	36	38	40	42	42	43
MED030	623045.5	4606973	39	40	49	62	72	77	80	80	81	81
MED031	623056.3	4606988	33	33	31	33	36	39	42	44	45	46
MED032	623049	4606948	39	36	30	29	30	31	32	33	34	34
MED033	623059.9	4606963	35	36	66	71	73	73	74	70	82	81
MED034	623070.7	4606977	37	35	26	26	27	29	30	31	32	32
MED035	623063.4	4606937	34	35	36	27	32	37	29	41	FAIL	FAIL
MED036	623074.2	4606952	76	78	78	79	80	81	81	81	81	84

Appendix B. Raw desiccant experiment data

B-1. Location 1

Site:	DES001	**Container weight (g):**	184
Easting : **(WGS84/NAD83 Z10T)**	622998.9	**Initial desiccant weight (g):**	705
Northing: **(WGS84/NAD83 Z10T)**	4607060	**Initial total weight (g):**	889

Measurement #	Time (PDT)	Total Weight (g)	Corrected[a] Total Weight (g)
0	09:55	889	889
1	10:24	892	890
2	10:54	890	891
3	11:27	898.5	892
4	11:57	902.5	893
5	12:30	881.5	894
6	12:35	889	894
7	13:35	886.5	896
8	15:04	910	899

[a] based on trendline described in section 3.2.1

B-2. Location 2

Site:	DES002	**Container weight (g):**	183.5
Easting : **(WGS84/NAD83 Z10T)**	623045.8	**Initial desiccant weight (g):**	558.5
Northing: **(WGS84/NAD83 Z10T)**	4607063	**Initial total weight (g):**	742

Measurement #	Time (PDT)	Total Weight (g)	Corrected[a] Total Weight (g)
0	09:57	742	742
1	10:27	747	744
2	10:59	744.5	745
3	11:31	754.5	747
4	12:01	752	748
5	12:36	756	750
6	13:37	740.5	753
7	15:06	760	758

[a] based on trendline described in section 3.2.1

B-3. Location 3

Site:	DES003	**Container weight (g):**	182.5
Easting : (WGS84/NAD83 Z10T)	623027.6	**Initial desiccant weight (g):**	514
Northing: (WGS84/NAD83 Z10T)	4607009	**Initial total weight (g):**	696.5

Measurement #	Time (PDT)	Total Weight (g)	Corrected[a] Total Weight (g)
0	09:58	696.5	696.5
1	10:31	694.5	698
2	11:03	695	700
3	11:35	704.5	702
4	12:05	700.5	704
5	12:40	697	706
6	13:39	712	710
7	15:07	720.5	715

[a] based on trendline described in section 3.2.1

B-4. Location 4

Site:	DES004	**Container weight (g):**	184
Easting : (WGS84/NAD83 Z10T)	623059.9	**Initial desiccant weight (g):**	619.5
Northing: (WGS84/NAD83 Z10T)	4606963	**Initial total weight (g):**	803.5

Measurement #	Time (PDT)	Total Weight (g)	Corrected[a] Total Weight (g)
0	10:00	803.5	803.5
1	10:35	823	809
2	11:09	814.5	813
3	11:39	826.5	818
4	12:08	820.5	822
5	12:46	824.5	827
6	13:49	837	836
7	15:08	844.5	848

[a] based on trendline described in section 3.2.1